

Investigation of background electron emission in the LUX detector

D.S. Akerib,^{1,2} S. Alsum,³ H.M. Araújo,⁴ X. Bai,⁵ J. Balajthy,⁶ A. Baxter,⁷ E.P. Bernard,⁸ A. Bernstein,⁹
 T.P. Biesiadzinski,^{1,2} E.M. Boulton,^{8,10,11} B. Boxer,⁷ P. Brás,¹² S. Burdin,⁷ D. Byram,^{13,14}
 M.C. Carmona-Benitez,¹⁵ C. Chan,¹⁶ J.E. Cutter,⁶ L. de Viveiros,¹⁵ E. Druskiewicz,¹⁷ A. Fan,^{1,2} S. Fiorucci,^{10,16}
 R.J. Gaitskell,¹⁶ C. Ghag,¹⁸ M.G.D. Gilchriese,¹⁰ C. Gwilliam,⁷ C.R. Hall,¹⁹ S.J. Haselschwardt,²⁰
 S.A. Hertel,^{21,10} D.P. Hogan,⁸ M. Horn,^{14,8} D.Q. Huang,¹⁶ C.M. Ignarra,^{1,2} R.G. Jacobsen,⁸ O. Jahangir,¹⁸
 W. Ji,^{1,2} K. Kamdin,^{8,10} K. Kazkaz,⁹ D. Khaitan,¹⁷ E.V. Korolkova,²² S. Kravitz,¹⁰ V.A. Kudryavtsev,²²
 E. Leason,²³ B.G. Lenardo,^{6,9} K.T. Lesko,¹⁰ J. Liao,¹⁶ J. Lin,⁸ A. Lindote,¹² M.I. Lopes,¹² A. Manalaysay,^{10,6}
 R.L. Mannino,^{24,3} N. Marangou,⁴ D.N. McKinsey,^{8,10} D.-M. Mei,¹³ M. Moongweluwana,¹⁷ J.A. Morad,⁶
 A.St.J. Murphy,²³ A. Naylor,²² C. Nehrkorn,²⁰ H.N. Nelson,²⁰ F. Neves,¹² A. Nilima,²³ K.C. Oliver-Mallory,^{8,10}
 K.J. Palladino,³ E.K. Pease,^{8,10} Q. Riffard,^{8,10} G.R.C. Rischbieter,²⁵ C. Rhyne,¹⁶ P. Rossiter,²²
 S. Shaw,^{20,18} T.A. Shutt,^{1,2} C. Silva,¹² M. Solmaz,²⁰ V.N. Solovov,¹² P. Sorensen,¹⁰ T.J. Sumner,⁴
 M. Szydagis,²⁵ D.J. Taylor,¹⁴ R. Taylor,⁴ W.C. Taylor,¹⁶ B.P. Tennyson,¹¹ P.A. Terman,²⁴ D.R. Tiedt,¹⁹
 W.H. To,²⁶ L. Tvrznikova,^{8,10,11} U. Utku,¹⁸ S. Uvarov,⁶ A. Vacheret,⁴ V. Velan,⁸ R.C. Webb,²⁴
 J.T. White,²⁴ T.J. Whitis,^{1,2} M.S. Witherell,¹⁰ F.L.H. Wolfs,¹⁷ D. Woodward,¹⁵ J. Xu,^{9,*} and C. Zhang¹³

¹SLAC National Accelerator Laboratory, 2575 Sand Hill Road, Menlo Park, CA 94205, USA

²Kavli Institute for Particle Astrophysics and Cosmology,
 Stanford University, 452 Lomita Mall, Stanford, CA 94309, USA

³University of Wisconsin-Madison, Department of Physics,
 1150 University Ave., Madison, WI 53706, USA

⁴Imperial College London, High Energy Physics, Blackett Laboratory, London SW7 2BZ, United Kingdom

⁵South Dakota School of Mines and Technology, 501 East St Joseph St., Rapid City, SD 57701, USA

⁶University of California Davis, Department of Physics, One Shields Ave., Davis, CA 95616, USA

⁷University of Liverpool, Department of Physics, Liverpool L69 7ZE, UK

⁸University of California Berkeley, Department of Physics, Berkeley, CA 94720, USA

⁹Lawrence Livermore National Laboratory, 7000 East Ave., Livermore, CA 94551, USA

¹⁰Lawrence Berkeley National Laboratory, 1 Cyclotron Rd., Berkeley, CA 94720, USA

¹¹Yale University, Department of Physics, 217 Prospect St., New Haven, CT 06511, USA

¹²LIP-Coimbra, Department of Physics, University of Coimbra, Rua Larga, 3004-516 Coimbra, Portugal

¹³University of South Dakota, Department of Physics, 414E Clark St., Vermillion, SD 57069, USA

¹⁴South Dakota Science and Technology Authority,
 Sanford Underground Research Facility, Lead, SD 57754, USA

¹⁵Pennsylvania State University, Department of Physics,
 104 Davey Lab, University Park, PA 16802-6300, USA

¹⁶Brown University, Department of Physics, 182 Hope St., Providence, RI 02912, USA

¹⁷University of Rochester, Department of Physics and Astronomy, Rochester, NY 14627, USA

¹⁸Department of Physics and Astronomy, University College London,
 Gower Street, London WC1E 6BT, United Kingdom

¹⁹University of Maryland, Department of Physics, College Park, MD 20742, USA

²⁰University of California Santa Barbara, Department of Physics, Santa Barbara, CA 93106, USA

²¹University of Massachusetts, Amherst Center for Fundamental
 Interactions and Department of Physics, Amherst, MA 01003-9337 USA

²²University of Sheffield, Department of Physics and Astronomy, Sheffield, S3 7RH, United Kingdom

²³SUPA, School of Physics and Astronomy, University of Edinburgh, Edinburgh EH9 3FD, United Kingdom

²⁴Texas A & M University, Department of Physics, College Station, TX 77843, USA

²⁵University at Albany, State University of New York,
 Department of Physics, 1400 Washington Ave., Albany, NY 12222, USA

²⁶California State University Stanislaus, Department of Physics, 1 University Circle, Turlock, CA 95382, USA
 (Dated: May 26, 2022)

Dual-phase xenon detectors, as currently used in direct detection dark matter experiments, have observed elevated rates of signals from electron emission processes in the low energy region. While this background negatively impacts detector performance in various ways, its origins have only been partially studied. In this paper, we report a systematic investigation of the electron pathologies observed in the LUX dark matter experiment. We characterize different electron populations based on their emission intensities and their correlations with preceding energy depositions in the detector. By studying these electron backgrounds under different experimental conditions, we identified the possible mechanisms that may contribute to the electron emission. We report the observed electron event rate in LUX after background rejection, and discuss how such backgrounds can be further mitigated in ongoing and future xenon-based dark matter experiments.

Keywords: dual-phase xenon time projection chamber, electron emission, noble liquid, low-threshold detector

I. INTRODUCTION

The dual-phase xenon time projection chamber (TPC) is one of the few particle detection technologies to have demonstrated sensitivities to single ionization electrons [1–4]. In liquid xenon, it only takes ~ 15 eV energy for electron recoils [5, 6], or ~ 250 eV for nuclear recoils [7], to produce one ionization electron. Through proportional electroluminescence (EL) amplification in xenon gas driven by strong electric fields, an electron can produce hundreds to thousands of secondary photons [8]. A typical xenon TPC used in dark matter search experiments can detect a few dozen EL photons for each electron [9–12], and higher electron gain values of $\gtrsim 100$ photoelectrons (PHE)/ e^- have also been demonstrated [13, 14]. The observation of single electron (SE) events not only provides an *in-situ* calibration for the experiments, but also enables them to have obtained world-leading sensitivities to GeV- and sub-GeV-mass dark matter candidates, substantially below the mass range targeted by these detectors [10, 15, 16].

Despite the exceptionally low background rates achieved in these underground experiments for energy depositions at the keV level and above, xenon TPCs exhibit elevated rates of electron and few-electron backgrounds similar to those expected from small energy depositions [10, 15, 17, 18]. This electron background negatively impacts the performance of xenon TPCs. For example, spurious electron (or few-electron) pulses can be incorrectly identified as true ionization events, or part of such events, causing inaccurate energy estimation and compromising detector energy resolution [19]. In addition, due to their high rates and large pulse areas, these electrons generate excessive triggers and pose a significant burden on the data acquisition, storage and processing systems of xenon TPC experiments. Most importantly, this background may impair the ability of xenon TPCs to search for ultra-low energy interactions to which these detectors are otherwise sensitive. This problem is most notable in rare event searches that rely on the high-gain ionization signals when scintillation signals are absent or at the detection limit [10, 15, 20, 21]. Although preliminary successes have been demonstrated, the excess rate of ionization-like background has so far prevented higher sensitivities at low energies from being reached.

Several authors have studied electron emission in xenon TPCs, and developed viable hypotheses that explain certain background populations [9, 11, 17, 18, 22–25]. In this work, we strive to obtain a coherent picture of these background effects through a systematic investigation of all observed electron pathologies in the Large Underground Xenon (LUX) dark matter exper-

iment [26]. The LUX detector was a low-background xenon TPC operated 4850 feet below the surface at the Sanford Underground Research Facility (SURF) between 2013 and 2016. Previous LUX work has produced several world-leading limits on dark matter interactions and other rare event searches [27–29], and developed calibration and analysis techniques that have since been widely adopted in this field [12, 19, 30–33].

The LUX experiment produced a wealth of information needed for a thorough electron background study. First, LUX achieved a low background rate of a few counts per second (CPS) in the 250 kg active xenon volume from internal and external radioactivities, which leaves large time intervals between particle interactions for pathological electron emission to be studied. Second, the LUX data acquisition system allowed all PMT outputs, including photoelectron (PHE) and SE pulses, to be continuously recorded for investigation of low energy events [34]. Third, over the three-year life span, LUX underwent a range of operating conditions, including various source calibrations, evolving impurity concentrations in the liquid xenon, and distinct electric field configurations throughout the active volume [35]. These expansive data sets enable correlations between operation conditions and electron background behaviors to be studied, so that different hypotheses of electron emission mechanism can be tested. Based on our improved understanding of the backgrounds, we evaluated the residual event rate of LUX in the few-electron energy region after new analytical cuts, and discuss the implication of this work for ongoing and future low-energy dark matter searches.

This paper is organized as follows: Section II reviews the possible charge production and migration mechanisms in dual-phase xenon TPCs; Section III to VI describe each population of the electron background observed in LUX, characterize their emission behaviors under varying experimental conditions, and discuss possible mechanisms that may be responsible for the production of these electrons; in Section VII, we study the residual electron rate in LUX after background rejections and discuss the impact of this work on dark matter searches; Section VIII concludes this work.

II. IONIZATION PHENOMENA IN LUX

The LUX detector contained 370 kg of pure xenon in a double-walled cryostat, which was hosted in a 7.6 m (diameter) by 6.1 m (height) water tank in the Davis Cavern of SURF. The central 250 kg of the liquid xenon, enclosed in an electric field cage, defined the active target volume of the TPC. Particle interactions with liquid xenon produce both scintillation photons and ionization electrons. In a LUX-style dual-phase TPC as illustrated in Fig-

* Corresponding author, xu12@llnl.gov

ure 1, scintillation photons (the so-called ‘S1’ or primary scintillation signal) are directly collected by two arrays of photomultipliers (PMTs) above and below the active volume. Ionization electrons are drifted upward and are extracted into the gas by the applied electric fields in the TPC. As electrons accelerate in the gas under the field, they produce secondary EL photons that are collected by the PMTs (referred to as the S2 or secondary EL signal). Combining the associated S1 and S2 signals, one can obtain information about the energy, position and interaction type of the events. More information about the LUX detector can be found in [26].

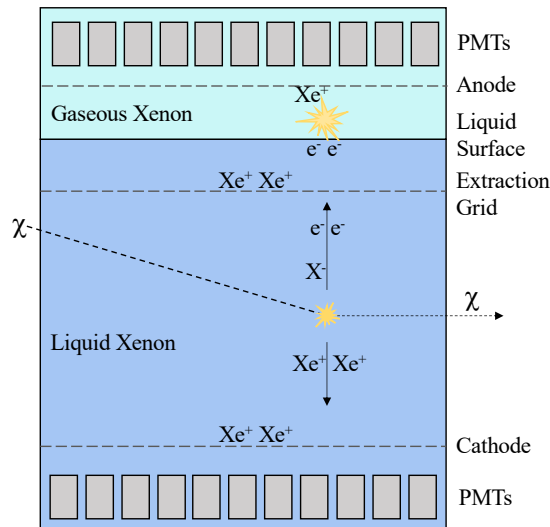


FIG. 1. A schematic illustration of a dual-phase xenon TPC such as LUX, including the major charge production and migration schemes inside the two-phase system.

In an ideal scenario, all ionization electrons produced in the liquid xenon would propagate to the gas phase and be detected. In reality, however, a fraction of the electrons are lost or temporarily trapped. First, electronegative impurities in liquid xenon can capture electrons and cause the detectable ionization signal to decrease exponentially with the drift time of the ionization clouds. In the LUX WIMP-search data acquired in 2013 (WS2013), the electron lifetime value was measured to vary between a few hundred microseconds and approximately one millisecond. At a typical electron lifetime of $750 \mu\text{s}$, approximately 35% of ionization electrons from interactions near the bottom of the TPC (maximum drift time of $325 \mu\text{s}$) were captured by impurities. The newly formed negative ions (denoted as ‘ X^- ’ in Figure 1) may drift in the detector under the effect of electric fields or the liquid flow, or neutralize in the metal spillover reservoir as xenon circulated through the purification system. Secondly, electrons arriving at the liquid surface can only be extracted into the gas if they have

sufficient kinetic energy to overcome the energy barrier at the phase boundary [36–38]. In WS2013, the electron extraction efficiency was measured to be $49 \pm 3\%$, and it was improved to $73 \pm 4\%$ for LUX data taken from 2014 to 2016 (WS2014–16) [29]. Unextracted electrons are thus trapped under the liquid surface; they may migrate to the wall, spill into the reservoir, or become captured by impurities and then drift with the liquid flow. Given sufficient excitation energy, these impurity-captured and surface-trapped electrons may be liberated and become a background [18].

While charge production and migration in xenon are usually discussed in the context of ionization electrons, it is important to also consider the corresponding positive ions produced. These positive ion clouds are expected to drift down to the cathode under electric fields, but they will also migrate with the liquid flow, in much the same way as negative ions. Moreover, extracted electrons may produce additional ionizations in the gas as they accelerate, especially in the high electric field regions near the anode grid wires; these resulting ions then drift downward under the effect of applied electric fields to the liquid surface, and possibly into the liquid. If the ions manage to reach the electrode grids, they may neutralize once in contact with metal or accumulate on the surfaces if neutralization is prevented from occurring.¹ The ion neutralization process may produce Auger neutralization electrons to discharge the combination energy [40]. This process may occur in the liquid, at the liquid surface, or on metal surfaces.

Particle interactions with xenon near detector surfaces lead to very different electric charge behaviors. Dielectric materials such as polytetrafluoroethylene (PTFE) reflectors may attract free charges near their surfaces and cause incomplete electron collection. Radioactive decays on electrode grid surfaces, where the electric field can reach very high values due to the relatively small surface area, usually result in highly suppressed and obscured scintillation signals and enhanced ionization signals that may be detected as pure charge events.

In addition to charge production by ionizing particles, free charges may also be generated in LUX from instrumental effects. For example, the ultraviolet xenon scintillation and EL photons carry an energy of $\sim 7 \text{ eV}$, which is above the work function of many metals and other species; therefore, the photoelectric effect can liberate electrons from the electrode surfaces and certain impurities dissolved in the liquid xenon [9, 11, 41]. In addition, electrons may be emitted from the cathodic electrode wire surfaces, where the electric field can reach very high values if physical or chemical defects are present [24, 42]. Electron emission from electrodes can lead to high voltage instabilities or even breakdowns and has prevented several TPC experiments from operating at the designed field configurations [35, 43].

¹ The barrier for ion neutralization can be oxide layers or mono-

layers of solid xenon formed on metal surfaces [39].

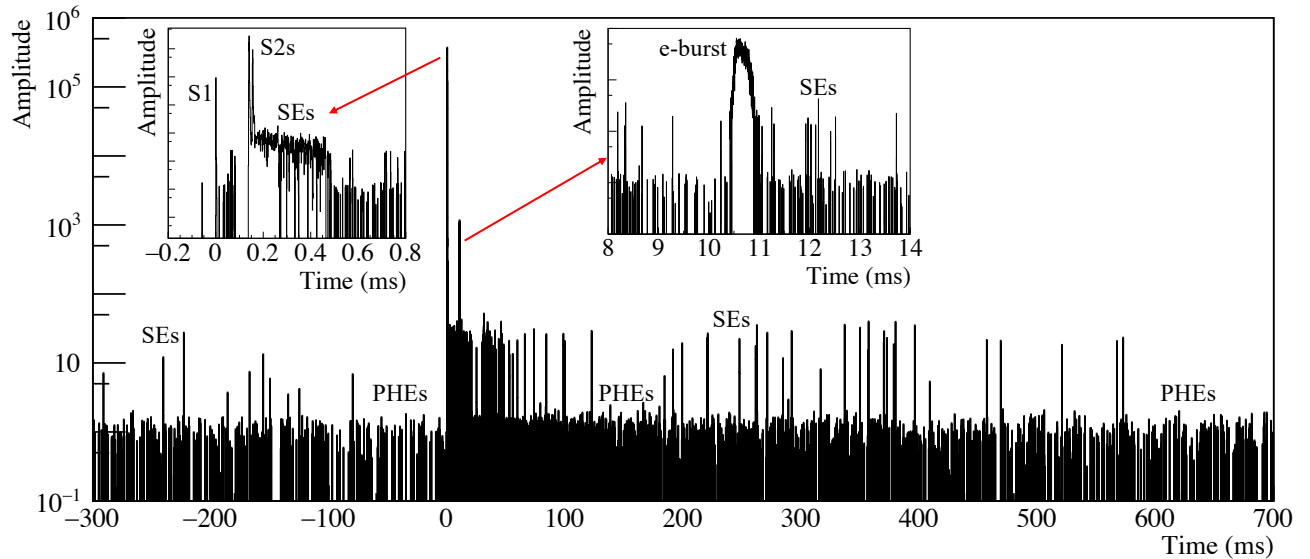


FIG. 2. A continuous LUX waveform over one second. Within this time window, only one 2.3 MeV gamma ray interacts with LUX but thousands of background electrons are observed to follow the S1 and S2 pulses. The insets show zoomed-in views of the S1-S2 event window and a tail window that contains an electron cluster (“e-burst”) and sparse single electron (SE) pulses and photoelectron (PHE) pulses. The summed and calibrated PMT traces have been re-binned to differentiate SEs from PHEs. In this scale, pulses with amplitudes near 1 are PHEs and pulses with amplitudes around 20 are SEs. Due to the coarse binning used in the time axes, typical S1/S2/SE/PHE pulses are seen as individual lines.

III. OVERVIEW OF ELECTRON BACKGROUND IN LUX

With a rate of 3–4 CPS in the whole active liquid xenon volume above a few keV, consecutive particle interactions in LUX are typically separated by hundreds of milliseconds. These long interaction-free windows allow delayed electron emission to be studied at timescales far exceeding the typical analysis event window (1 ms). Figure 2 shows a continuous LUX waveform over a one-second period. The interactions of a 2.3 MeV gamma ray with liquid xenon lead to the detection of 9,300 prompt photons and 41,000 electrons. Following the S1 and S2 pulses, an increased population of electrons and photons emerge, which lasts for hundreds of milliseconds and into the next interaction event. The background comprises mostly sparse SE and PHE pulses, but may also contain intense clustered electron emission. This apparent time correlation leads us to conclude that these electrons are produced by the prior, relatively higher energy interactions that precede them. In the following sections, we examine possible production mechanisms for these induced electrons and electron clusters.

Based on the emission characteristics of the background electrons and their time correlation with preceding events, we place them in three categories: 1) photoionization electrons that occur immediately after the S1 and S2 pulses, 2) clustered electron emission that consists of multiple electron pulses in short periods of time,

and 3) delayed emission of individual electrons. In the following sections we will quantitatively describe the electron populations and study their correlations with experimental operation conditions so that connections between these emission processes and the ionization phenomena presented in Section II can be made.

This work primarily uses LUX WS2013 data unless specified otherwise. Unlike previous LUX studies that used the same data set, the analysis framework is completely redesigned for the efficient identification and parametrization of small pulses such as SEs and PHEs. In particular, this work is independent of the LUX event-building system, and treats all recorded PMT waveforms as a continuous stream of pulses.² Special care was given to baseline corrections, pulse finding and splitting of closely overlapped pulses. Thousands of waveforms were visually scanned, and we estimate an efficiency of >95% for identifying SE and PHE pulses in the analysis. The additional loss of efficiency due to the internal digitizer thresholds is negligible, estimated to be 5% for PHEs [34]. For position reconstruction of S2s, instead of using the sophisticated Mercury algorithm [33], a less computation-intensive method was developed that uses only the group of 7 neighboring PMTs with the most detected light in the top PMT array (3 or 4 PMTs for events at the perimeter of LUX). A comparison to standard LUX results indicates a modest degradation of the

² Dead-time in recorded LUX data is $\mathcal{O}(0.1\%)$, or 2–3 ms for every ~ 2 s data acquisition window.

position resolution (σ) from 2.1 cm to 2.9 cm for SE pulses. To evaluate the areas of large S2 pulses that saturate top-array PMTs, we use the bottom PMT array area with a correction based on the unsaturated top-bottom PMT signal ratio. In all following analyses, we will quantify background descriptions whenever possible, but a full study of uncertainties is beyond the scope of this work.

IV. PHOTOIONIZATION ELECTRONS

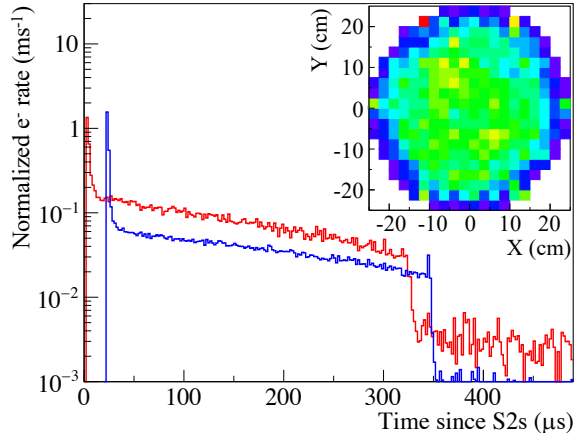


FIG. 3. The distribution of SE detection time after thousands of selected ^{83m}Kr -decay S2s at low (red) and high (blue) electron lifetime values, plotted as the electron pulse area divided by the S2 area. The peaks near 0 and 325 μs are mostly from photoelectric effects on the electrode surfaces, and the continuous distribution in between is from photoionization in the liquid. The blue histogram is offset by +20 μs for display of the peaks. The inset shows the horizontal (X-Y) position distribution of SEs detected within 10–320 μs after ^{83m}Kr S2s of $r < 10$ cm.

As illustrated in the inset of Figure 2 (top left), a prominent electron background population is observed immediately after S2 pulses. This background is comprised of individual electron pulses with a rate that decreases with time. In the case of large S2s, a sharp drop in the electron rate is usually observed at 325 μs —the maximum drift time in LUX—after the S2 time. Figure 3 shows the arrival time of electron pulses and their X-Y positions (inset) following ^{83m}Kr calibration decay events [32]. The rate of electrons increases with S2 pulse area and also with impurity concentration in the liquid xenon, measured by the electron lifetime (inverse of the probability for an electron to be captured by impurities in liquid xenon per unit drift time). Based on these observations, the immediate electrons (time delay < 325 μs) are attributed to the photoionization by S2 light on impurities dissolved in liquid xenon. This phenomenon has been observed and discussed in other xenon TPC experiments including ZEPLIN-II [1], ZEPLIN-III [9] and XENON100 [11].

A. Photoionization yield

This immediate electron emission occurs not only following S2s, but also following S1s, consistent with the photoionization explanation. Figure 4 (left) shows the time distribution of SEs in the tail of S1s, where the electron rate is calculated as the ratio of electron pulse area to the S1 area. To isolate the features particular to S1 photoionization from S2-related backgrounds, we select only xenon interaction events below the LUX cathode. In these events, the nominal S2 pulses are not detected because the ionization electrons are drifted downward by the reversed electric field (referred to as ‘S1-only’ events hereafter despite the S1 may produce spurious electron pulses), but their positions can be indicated by the dominant S1 signal recorded in the bottom array PMTs. In contrast to SEs following S2s, the rate of SEs following S1s increases with time, up to 325 μs . This behavior is more apparent after a correction for the electron loss to electronegative impurities during drifts has been applied. This difference is explained by the locations of the light source, which is at the bottom of LUX for the S1-only studies and at the top for the S2 studies.

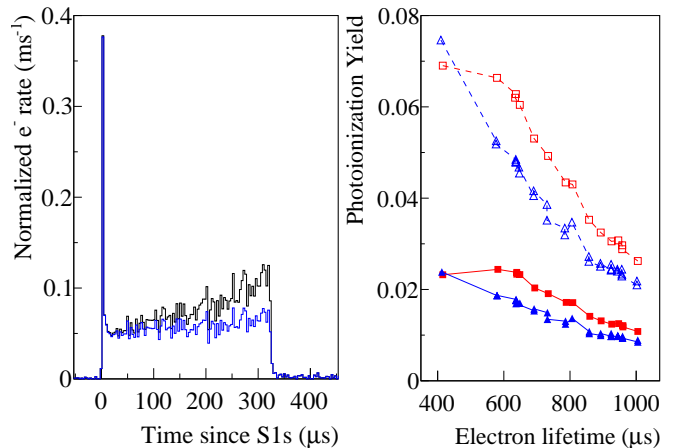


FIG. 4. **Left:** The electron pulse rate after S1-only events, normalized to the S1 area. The blue histogram is the observed rate and the black includes a correction for electron loss during drift. The peak near $t \sim 0$ is from photoelectric effect on the extraction grid. **Right:** The photoionization yield (total area of photoionization electrons, divided by the S1 or S2 pulse area) for S1s (blue triangles) and S2s (red squares) as a function of electron lifetime. Both the raw yield values (solid markers) and those corrected with electron loss to impurities and extraction efficiency (hollow markers) are plotted. Uncertainties on the data points are estimated to be at the level of 10% of the corresponding values. The lines connecting the data points are not suggestive of any interpolation models, but serve illustrative purposes by keeping the data grouped.

As shown in Figure 4 (right), the photoionization yields for S1s and S2s are comparable, in the range of 1–10%, both decreasing at high xenon purities. The raw yield value is the ratio of the electron pulse area in the 20–

320 μ s delay window following the S1 or S2 pulses to the S1 or S2 pulse areas. The corrected yield value accounts for the electron losses to impurities and incomplete extraction into the gas (49% in these data). The higher yield values for S2s are mostly due to other electron backgrounds following S2s (Sec. VI). To reduce this contamination, we only select ^{83m}Kr decays within the top 5 cm of liquid xenon, where the additional background is relatively small, in the calculation for S2 photoionization yield. We also require no other interaction events in the 10 ms window before the S1 or S2 pulses under study to minimize contamination from previous energy depositions in the detector.

In the following quantitative discussions, we will focus on the S1-only events, taking advantage of their clean photoionization features. Given an average SE size of 25.9 PHE/ e^- ,³ a photon detection efficiency of 13% for light emitted below the cathode, and a mean total path length of approximately 2 meters for photons in the LUX liquid xenon predicted by simulations [45], the observed photoionization yield translates to an electron production rate of $(5\text{--}20)\times 10^{-5} e^-/\gamma/\text{m}$ in LUX. Assuming an ionization quantum efficiency of $\mathcal{O}(1)$, the corresponding effective photon attenuation length is at the order of 10 kilometers, which is in agreement with a similar calculation in Ref. [22]. The photoionization process is a subdominant channel for photon extinction in the bulk liquid xenon since the LUX light collection efficiency remained unchanged when the photoionization yield varied by a factor of 4 at different purity levels.

In addition to photoionization in liquid xenon, light from S1s or S2s can also produce photoelectrons on the metal grids that supply electric fields for the TPC operation. This is illustrated by the peak structures at $t\sim 0$ (extraction grid) in Figure 3 and 4 (left) and at $t\sim 325 \mu\text{s}$ (cathode) in Figure 3. No cathode photoelectron peaks are observed to follow S1-only events because the photons mostly strike the electrode wires from below; as a result, the liberated electrons will primarily drift downward and cannot be detected. The cathode peak is not observed in some low xenon purity data (such as red histogram in Figure 3) because of the large photoionization population and the strong absorption of electrons from the bottom of LUX by impurities. The extraction grid photoelectron peak ($t\sim 0$) in Figure 4 (left) integrates to $\sim 0.1\%$ of the detected S1 area. With optical simulations using GEANT4 [45, 46], we estimate that 2.3% of the below-cathode scintillation light is absorbed by the extraction grid, leading to a SS304 stainless steel quantum efficiency of $\sim 4\times 10^{-4}$ for 7 eV photons. In this calculation we assume that all photoelectrons from the extraction grid

surfaces drift upward and can be detected, an approximation supported by electrostatic field simulations using COMSOL [35, 47]. Similar calculation for the cathode (SS302) photoelectrons produced by S2 yielded quantum efficiency values of the same order of magnitude, but these carry large uncertainties due to the contamination from additional electron backgrounds and the uncertainty in the fraction of photoelectrons that can be detected. This obtained quantum efficiency value is higher than that reported for stainless steel (unspecified grade) by a factor of 2 [48]. This increase is mostly explained by the reduction of the effective work function of the metal by the electron affinity of liquid xenon [49, 50]; the contribution from Schottky effect in reducing the steel work function is subdominant (10 times smaller than the liquid xenon affinity effect) for the electric fields on the grid surfaces in LUX. Other possibilities include differences in the stainless steel grades, the accumulation of positive ions on the grid surfaces [51], and changes to the electrode surface composition due to collection of positively charged impurities from the liquid.

B. Photoionization centers in liquid xenon

Although the photoionization process in liquid xenon has been discussed by several authors, little is known about the ionization centers other than their connection to electronegative impurities [1, 9, 11, 22, 41]. An often-discussed candidate for photoionization is negatively charged impurities, such as O_2^- , which are formed after electron captures on the electronegative species. These negative ions can have a relatively low ionization energy of <1 eV, while neutral impurity molecules such as O_2 , N_2 and H_2O usually have ionization energies above 10 eV, which appears incompatible with the energy of S1 or S2 photons [52, 53]. This hypothesis may be tested with LUX data from two different perspectives.

First, if negative ions are responsible for the photoionization emission, the photoionization yield should increase with the negative ion concentration in the liquid. The LUX detector was frequently calibrated with internal and external sources, which produced increased rates of ionization. During these periods, the rate of negative ion formation through captures of drifting electrons also increased. Figure 5 (top) shows the varying rates of ionization electrons detected in LUX for background data (30,000 e^-/s), ^{83m}Kr calibration data (40,000–50,000 e^-/s), and deuterium-deuterium neutron calibration data (200,000–250,000 e^-/s). Despite the significant changes in the expected negative ion formation rate, the S1 photoionization yield remains stable at the 10% level. We comment that negative ions such as O_2^- drift at a speed of 2 mm/s in liquid xenon at the LUX field (180 V/cm) [54], so they could all migrate to the liquid surface within several minutes; therefore, the negative ion formation rate can be a good indicator for the

³ The PMT calibration in this work does not compensate for the multi-photoelectron effect [44] because we study both xenon scintillation light and non-xenon photon background (Sec. VI). Therefore, this SE gain value is slightly different from that used in other LUX analyses.

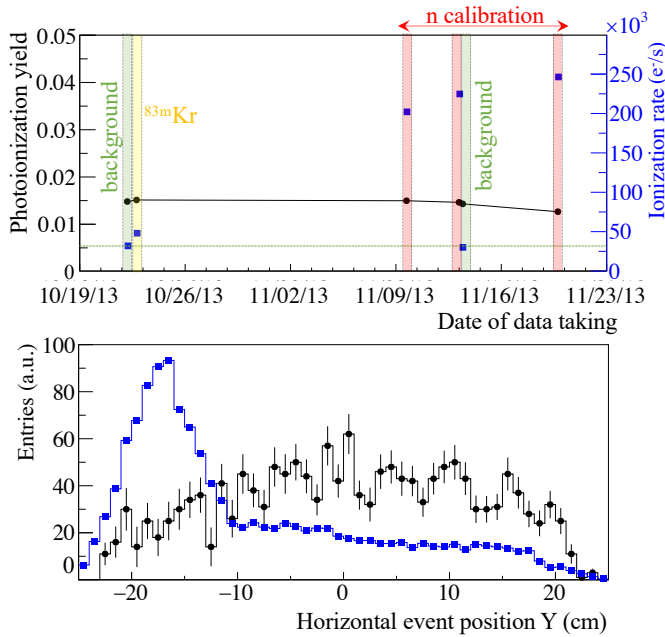


FIG. 5. **Top:** The S1 photoionization yield values (left scale) and the detected ionization rates (right scale) in LUX under different operating conditions. The photoionization yield values are corrected for evolving electron lifetime using Figure 4 (right). The neutron calibrations were carried out intermittently between November 10th and 21st in 2013 (>50% duty cycle). **Bottom:** The Y position distribution for S1 photoionization electrons (black dots) and for total ionization electrons (blue squares) during neutron calibration. The Y direction defined in LUX is approximately parallel to the incident neutron direction and lies in the horizontal plane.

negative ion concentration in the liquid.⁴

Second, the three-dimensional positions of the photoionization electrons can be reconstructed and compared to that expected for negative ions. Figure 5 (bottom) compares the Y positions of S1-induced photoionization electrons (black dots) to that of detected ionization events (weighed by number of electrons) in neutron calibration data (blue squares). Although the local energy deposition near the neutron beam entry into the xenon volume ($y \sim -20$ cm) increased by a factor of 10, the horizontal position distribution of photoionization electrons does not exhibit any significant enhancement in this region. The Z position of the photoionization electrons also remains consistent with Figure 4 (left) although the additional radiation during neutron calibration was primarily delivered to the upper half of the detector. Further, the Z distribution of photoionization electrons as shown in Figure 3 and Figure 4 (left) can be approximately reproduced with optical simulations [45] that assume a homogeneous distribution of ion-

ization centers throughout the liquid xenon. It is worth noting that negative ions are expected to have higher concentrations in the upper part of the liquid volume in all configurations because more electron are captured in this region and because negative ions formed in the bottom are expected to drift upward under the influence of the applied electric field.

In the above discussions, we implicitly assumed that the LUX liquid xenon body was static and charge transport in the detector was solely governed by the electric fields. However, Ref. [55] suggests that convection effects may lead to a liquid flow speed as high as 3 cm/s in certain regions of the detector, measured using delay coincidence of radioactive-chain decays. If this pattern persisted throughout the LUX operation, the convection flow could have reduced the inhomogeneity in the negative ion position distributions, easing the tension from the position comparisons, but the rate argument should still remain valid. In this scenario, the concentration of negative ions in LUX is no longer determined by the prompt production rate of negative ions but its integrated history. In LUX the xenon circulation turn-around time was 1–3 days, and during this process all ions should lose their charge states. Therefore, with approximately 10 days of neutron calibration (>50% duty cycle), the negative ion concentration should reach an equilibrium with the increased radiation level, and yet no significant changes in photoionization yield was observed. The purity-corrected yield values are stable at the level of 20% in all data sets studied for this test.

Based on these observations, we rule out negative ions from dominating the photoionization process, and, instead, propose that some neutral impurities must play a leading role. However, given the strong correlation between the photoionization yield and the electron lifetime, this neutral impurity should be present in proportion with the electronegative species. Therefore, the magnitude of this photoionization background can be used as a liquid xenon purity monitor in lieu of dedicated source calibrations, as successfully demonstrated by ZEPLIN-III [9], LUX [41] and XENON100 [11]. In addition, the single electron-ion pair produced by the photoionization effect can be easily separated by weak electric fields, and thus the electron collection efficiency is insensitive to modest changes in the local electric field, a behavior observed for low ionization density interactions in liquid xenon [14, 56]. Combining with the fact that SE pulses are unlikely to suffer signal distortions, the photoionization electrons can provide a robust charge collection efficiency calibration even in non-uniform electric fields.

V. CLUSTERED ELECTRON EMISSION

The most prominent electron emission pathology observed in LUX is clustered electron emission, as already illustrated in Figure 2 (top right inset). Such a cluster may contain a few dozens of consecutive electron pulses—

⁴ Section VI discusses evidence of negative ions releasing electrons, which also suggests that negative ions may deplete quickly.

and up to tens of thousands in some cases—in a time window of $10\ \mu\text{s}$ – $1\ \text{ms}$ that is preceded and succeeded by quiet periods. Because multiple electrons may be emitted at the same time, clusters with small numbers of pulses can pose a significant background for dark matter searches using S2-only events. Within large clusters, similar structures are often observed, with the rate of electron pulses slowly rising in the beginning and falling in the end. Despite large variations, the rise time and fall time are typically 10 – $100\ \mu\text{s}$, and the most probable peak widths (25%–75% integral) are approximately 30 – $50\ \mu\text{s}$, consistent with similar pathology events observed in XENON10 [57]. Usually no prompt scintillation pulses are observed to precede the clusters, which also differentiates them from typical particle interactions in liquid xenon. These clusters often closely follow the large S2 pulses arising from particle interactions in LUX ($<50\ \text{ms}$ delay) and share the same X-Y locations as these S2s. In the following discussions, this clustered electron background type will be referred to as ‘e-bursts’.

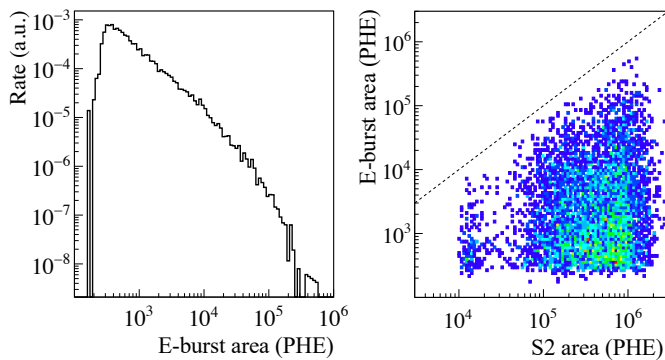


FIG. 6. **Left:** The energy spectrum of e-burst clusters observed in twenty hours of WIMP search data; **Right:** The summed e-burst area within a 50 ms window following an S2 as a function of the raw S2 area. The dashed line corresponds to equal e-burst area to the S2 area. For reference, the average SE area is 25.9 PHE.

Figure 6 (left) shows the e-burst area distribution in a twenty-hour WIMP-search data set. The spectrum is largely featureless, and decreases monotonically with the e-burst area; the low-energy cutoff below 300 PHE is due to the loss of tagging efficiency for small e-burst clusters that are difficult to distinguish from random pileups of SEs. The upper bound of e-burst area distributions, however, is observed to correlate with the area of preceding S2s, as illustrated in Figure 6 (right). In the data investigated, the maximum e-burst area values are typically 10–50% of that of preceding S2s. For large e-bursts, a single cluster can contain a number of electrons close to that of the preceding S2, but primarily consists of SE pulses dispersed over a large period of $\mathcal{O}(1\ \text{ms})$. Although most S2s do not produce e-bursts, a few percent of them are followed by multiple such clusters. In these rare cases, a large e-burst may appear before or after smaller ones despite that the large e-bursts on average have smaller time

delays from the correlated S2s. When evaluating the e-burst area for these events, we use the summed e-burst area in the 50 ms window following the S2s, but usually the sum is dominated by the largest cluster rather than the combined area of smaller ones.

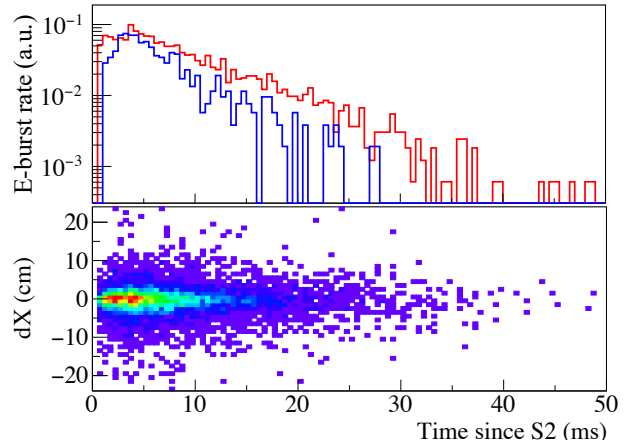


FIG. 7. **Top:** Time delay of e-bursts from their preceding S2s for interactions in the top (red) and bottom (blue) of LUX in one data set. Top and bottom here are defined as 5 cm below the liquid surface, and 5 cm above the cathode grid, respectively, while the liquid surface and cathode are separate by 49 cm in LUX. **Bottom:** The X position difference between e-bursts and preceding S2s, plotted as a function of the time delay. In these analyses, we require that there be no additional S2 pulses in the period of $[-30, +50]$ ms relative to the S2s of interest.

The distribution of time delay between e-bursts and their preceding S2s can be described by a single exponential, with a characteristic delay time of $<10\ \text{ms}$, as illustrated in Figure 7 (top). We comment that due to the Poisson nature of particle interactions, the time separation between an uncorrelated process in LUX and the preceding S2 pulse will also follow an exponential distribution, the decay constant of which (250–300 ms) is governed by the LUX event rate (3–4 CPS). In this analysis, by requiring only one S2 pulse in the time window under study, we have suppressed this superficial exponential component and thus can focus on real time correlations. The exponential nature of the e-burst time delay is consistent with a model where these electrons are supplied from a reservoir that is filled around the time of the S2s and is continuously drained at a fixed rate over time. Competing processes for draining this reservoir should exist; otherwise, the summed e-burst area should be more directly correlated with the preceding S2 area. Figure 7 (bottom) also shows the position difference between e-bursts and their preceding S2s as a function of the time delay. The electron pulses in a cluster usually share the same X-Y positions, which also coincide with that of preceding S2s. This position correlation does not appear to weaken over time up to 50 ms.

Based on the observed energy, time and position correlations between e-bursts and their preceding S2s, we

propose that this clustered electron emission may result from one of the direct electron sources discussed in Sec. II, including unextracted electrons and impurity-captured electrons. Hypotheses involving primary positive ion clouds are disfavored because of their small mobility in liquid xenon. With an estimated drift velocity of 8 mm/s at the LUX drift field [54], it would take minutes for a positive ion cloud to reach the cathode grids, and thus cannot explain the immediate emission of e-bursts (within ms after S2s). The ions that may be produced in the high-field gas regions near LUX anode wires could travel down to the liquid surface within a few milliseconds [58], but due to the fixed traveling distance, these ion activities should occur with a constant time delay from the S2s, rather than producing an exponentially decaying electron background. Ion neutralization with negative charges during drift may produce exponentially decaying rates if the neutralization probability is constant over time, but it should occur at a much longer timescale (seconds or longer) than is observed.

To further test these hypotheses, we quantitatively describe the e-bursts using their rate of decay over time and their characteristic size under different experimental conditions. We note that the average area does not provide a robust characterization of the e-burst size because it is dominated by the small e-bursts and is relatively insensitive to changes in the high-end tail, as evidenced by the drastic rate decrease at large e-burst areas shown in Figure 6 (left). Instead, we characterize its size using the 99-percentile e-burst area (an approximation to the maximum area) divided by the preceding S2 area, referred to as $R_{99\%}$, for this analysis. When calculating $R_{99\%}$, we also include S2s that are not followed by identifiable e-bursts, so this calculation is not biased by the inefficiency in tagging small e-bursts.

Figure 8 shows the decay time of e-bursts (top) and their $R_{99\%}$ values (bottom) at different liquid xenon purity (electron lifetime) levels; the results are separately plotted for interactions in the top (5 cm below the liquid surface) and bottom (5 cm above the cathode grid) of LUX, in WS2013 (49% electron extraction) and in WS2014-16 (73% electron extraction). Generally speaking, the e-burst emission becomes stronger and also last for longer as the liquid xenon purity, evaluated using the electron drift time, improves. Despite sharing similar purity dependence, particle interactions in different regions of the detector lead to different e-burst behaviors. Compared to e-bursts following interactions near the top of LUX, the decay of e-bursts following bottom-originating S2s occurs faster (Figure 7, top, blue line, and Figure 8, top, blue lines), and these e-bursts are on average smaller in size. This top-bottom disparity disfavors the impurity-captured electrons as an explanation for the e-burst emission, because bottom-originating ionization events produce more negatively charged impurities due to the longer electron drift, a trend contradicting the observation. Rather, the weakening of e-burst emission with higher concentration of impurities in liquid xenon

indicates that impurities are a competitor to e-burst productions. The same difficulty applies to other processes involving impurity-captured electrons such as the combination of positive and negative ion clouds.

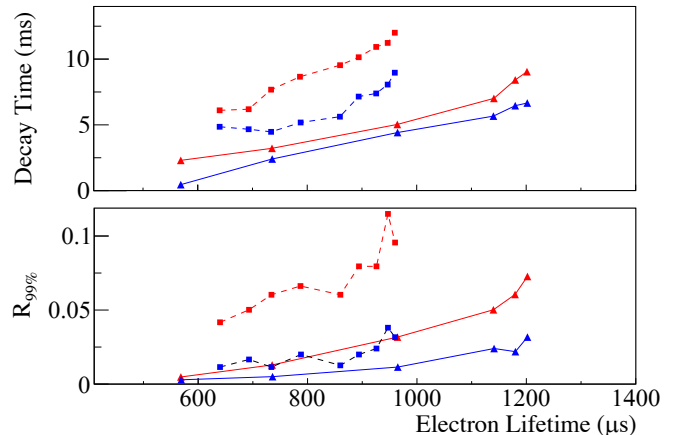


FIG. 8. **Top:** The observed decay time of e-burst clusters following interactions in the top (red) and bottom (blue) 5 cm of LUX liquid xenon in WS2013 (squares) and WS2014–16 (triangles). **Bottom:** The $R_{99\%}$ parameter (defined in the text) as a function of electron lifetime (same legend notation as the top subfigure). Uncertainties on the data points are estimated to be at the level of 10% of the corresponding values. The lines connecting the data points keep the data grouped for illustrative purposes.

Unextracted electrons trapped under the liquid surface provide a strongly favored electron source for e-bursts. In LUX WS2013 data, with an extraction electric field of 3.5 kV/cm below the liquid surface, approximately 49% of the ionization electrons arriving at the liquid surface were extracted into the gas while the rest became trapped. If these trapped electrons can emerge into the gas together under certain excitation mechanisms, the electron emission would be expected to exhibit energy, time and position correlations with preceding S2s similar to that observed for e-bursts. In addition, while the electrons are trapped under the liquid surface, they may also become captured by impurities and can no longer be excited, which naturally explains the decreased sizes of e-bursts and their faster extinction at high impurity levels. In this scenario, since e-bursts can only arise from surface-trapped electrons before they get captured, their sizes only correlate weakly with that expected of unextracted electrons and the distribution can have a significant spread, possibly matching Fig. 6. Further, as shown in Figure 8, an increased electron extraction efficiency in WS2014–16 (4.2 kV/cm extraction field, 73% efficiency) leads to fewer trapped electrons, and consequently the e-burst emission dies out more quickly and the e-burst size becomes smaller.⁵

⁵ Due to the evolving electric field distortion in WS2014–16, the

However, this explanation faces two difficulties: 1) how can quasi-free electrons preserve their X-Y positions under the liquid surface for tens of milliseconds, and 2) why is the electron lifetime at the liquid surface 5–10 times larger than that in the liquid bulk? These two challenges may be simultaneously addressed if a deformation of the liquid surface occurs where the electrons are trapped. The presence of dense electric charge under the liquid surface in a strong electric field can raise the local liquid level microscopically; this local liquid level deformation, together with the vertical electric field, can function as a physical trap and preserve the X-Y position of trapped electrons for a long time. At the same time, being trapped in a small volume could limit the exposure of these electrons to impurity molecules and alter the velocity-dependent capture cross section [59], so that the observed electron lifetime is significantly increased. Moreover, if this hypothesis is correct, higher density electron clouds, such as those from the top-originating ionization events where transverse diffusion is less significant, can produce stronger traps and thus explain the observed top-bottom disparity.

Regarding the underlying mechanism that may excite unextracted electrons to be emitted from the surface in clusters, one possibility is the movement of the liquid xenon surface, such as capillary waves, which may be generated by the xenon flow, formation of bubbles in liquid or other instrumental effects. The e-burst widths of $\lesssim 1$ ms correspond to an excitation frequency of kHz, which matches that of capillary waves for liquid xenon estimated from its surface tension [60]. Amid upward oscillations of the liquid surface, the trapped electrons gain kinetic energy from the strong electric field and at the same time dissipate part of the gained energy to xenon atoms through collisions. This process is in direct analogy with the heating of primary electron clouds when they first reach the liquid surface, and if sufficient energy is gained the electrons can be extracted into the gas [36]. In addition, the strongest e-burst emission region in LUX ($X \sim 0$, $Y \sim -23.5$ cm) coincides with the location of the largest detected S2 signal areas for mono-energetic ^{83m}Kr delays in the liquid [32], which also suggests unusual activities on the liquid xenon surface in this region. Other forms of delayed emission may also occur for these trapped electrons, such as thermionic emission [17], but no significant evidence for a fast emission component as reported in Ref. [18] is observed in this work.

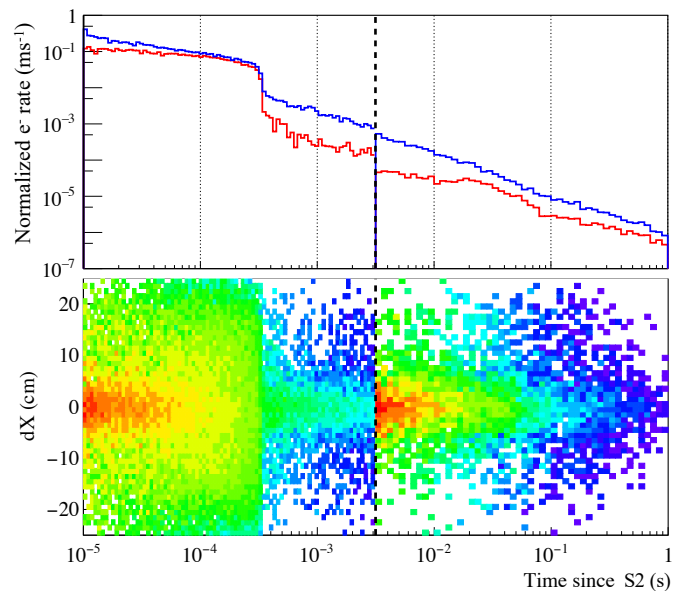


FIG. 9. **Top:** The relative electron background rate (normalized to the S2 signal area of the preceding event) as a function of delayed emission time. The red (blue) spectrum is for SEs following energy depositions in the top (bottom) 5 cm of active LUX liquid xenon. **Bottom:** The difference of X position between SEs and preceding S2s (near the center of LUX) as a function of delay time. Different sets of data are used to generate the plots < 3 ms and > 3 ms, leading to a small discontinuity. This transition is indicated by the vertical dashed line.

VI. DELAYED EMISSION OF INDIVIDUAL ELECTRONS

If one excludes the photoionization electrons and the e-burst emission, the remaining electron background in LUX lacks a clear timing structure. It mostly consists of SEs that in total account for less than a few percent of the preceding S2 area. The rate is observed to decrease monotonically with time since the preceding S2s, up to the longest timescale (1 second) that can be studied with LUX data. In the following analysis, we study this background population in two delay time windows: a) 0–3 ms and b) 3–1000 ms following S2s. For the short window (0–3 ms) analysis, we select ^{83m}Kr calibration events to obtain high statistics, and for the long window (3–1000 ms), we use low-background WIMP-search data so that longer electron delay times can be studied. In each scenario, we select the events that only contain one particle interaction with liquid xenon in the whole analysis window. As explained in Sec. V, this criterion is necessary to suppress the superficial exponential feature that arises from the Poisson nature of particle interactions in LUX. In addition, we require no other significant energy depositions in the preceding 100 ms so that contamination from earlier events is subdominant. Electrons that appear in e-burst-like clusters are excluded from this analysis.

calculation of drifting electron lifetime in LUX liquid using ^{83m}Kr decays carries an additional source of uncertainty. However, this statement should hold as long as the evaluated lifetime values are accurate within a factor of 2.

Figure 9 (top) shows the relative intensity of SEs—summed SE area (normalized to 1-millisecond integration windows) divided by the preceding S2 area—as a function of the time delay from the preceding S2 following events in the top (red) and in the bottom (blue) of LUX. Both spectra show similar time dependences, including a clear photoionization cutoff at the maximum S2 drift time of $325\ \mu\text{s}$ (Sec. IV) and a long power-law tail up to 1 s. At all delay time values, the SE rate is higher following interactions in the bottom of LUX compared to that in the top. In addition, the majority of this electron population exhibits a strong X-Y position correlation with the preceding S2s, as illustrated in the bottom of Figure 9. This position correlation rules out cascade photoionization (S2 - photoionization - SEs - photoionization, and so forth) as a significant contributor to this tail. The relatively low photoionization yield also means that the amplitude of this cascade should decrease by 1–2 orders of magnitude for every $325\ \mu\text{s}$ and will become insignificant after 1 ms.

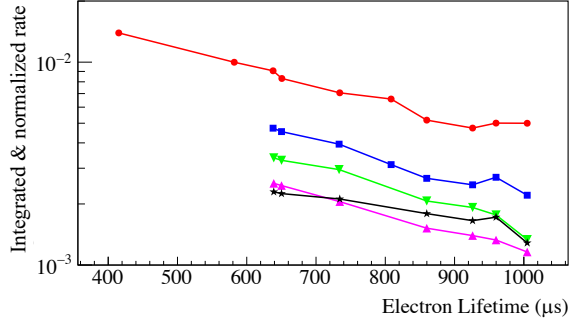


FIG. 10. The integrated SE background rates at varying liquid xenon purity levels (electron lifetime) associated with different periods of detector operation, calculated in different delay time windows after the S2: 10–500 μs (red dots), 500 μs –3 ms (blue squares), 3–10 ms (green downward triangles), 10–100 ms (purple upward triangles), 100–1000 ms (black stars). Uncertainties on the data points are estimated to be at the level of 10% of the corresponding values. Here we select only SEs after particle interactions in the bottom 5 cm of LUX because they produce the most delayed SEs. Data points for the delay window of 10–500 μs have the S2 photoionization contributions subtracted already. The lines connecting the data points only serve illustrative purposes by keeping the data grouped.

We further studied the dependence of this background rate on the liquid xenon purity, as summarized in Fig 10. In all delay time windows studied, the electron rate decreases as the electron lifetime increases. The dependence of SE rates on the Z position of preceding interactions (Fig. 9, top) and on the xenon purity (Fig. 10), together with the X-Y position correlation (Fig. 9, bottom), indicate that they may originate from electrons captured by impurities [18]. Ionization electrons produced by particle interactions near the bottom of LUX had to drift across large distances in liquid xenon and thus would leave behind more negatively charged impurities. Due

to their low expected mobility and diffusivity, negatively charged impurities can preserve their X-Y positions for a long time. So, if they can release the electrons under certain excitations, the resulting electrons will exhibit the observed behaviors.

A small fraction of the delayed SEs do not share X-Y positions with preceding S2s. In addition to photoionization electrons generated by EL photons from other SEs, this population may also include delayed electron emission by negative ions produced during earlier interactions in the detector. The subdominant rate of this population suggests that the responsible negative ions may be extinguished quickly in liquid xenon, either by releasing the electrons or through other processes (combining with positive ions with and without Auger neutralization electron emission, drifting to the liquid surface and spilling into the reservoir, attaching to detector surfaces, etc), supporting the hypothesis assumed in Sec. IV. As suggested in Ref. [18], thermal collisions could lead to the ionization of certain negatively charged impurities with an estimated time scale of seconds, possibly explaining this electron emission.

Another possibility for negatively charged impurities to release electrons is photoionization by background optical or infrared photons in LUX. As illustrated in Figure 2 and discussed in [21], an increase of the PHE rate is observed in LUX after energy depositions. The spectrum of these PHEs does not exhibit a significant double-photoelectron emission effect in LUX PMTs, suggesting that they have longer wavelengths than the vacuum ultraviolet (VUV) xenon photons associated with the regular S1 and S2 emission processes. Figure 11 (top) shows the PHE rate in the LUX detector following high-energy S2s. This plot is produced similarly to Figure 9 (top), but we further require the PHE pulses are not in the immediate vicinity of (1 μs before and after) SEs or S2s to exclude misidentified photons that are part of SE or S2 pulses. Similar to SEs, the PHE rate exhibits a gradual power-law decrease over time. Beyond 325 μs past the S2 time, the ratio of the PHE rates in the top PMT array to that in the bottom array remains approximately 1:2, leading to a top-bottom asymmetry (T-BA) value $(A_T - A_B)/(A_T + A_B) = -0.3$ (Figure 11 bottom). This observation disfavors the explanations of these PHEs as thermionic dark noise or other PMT instrumental effects due to the equal PMT numbers in the two arrays and the higher VUV photon signal rate in the top array. If we assume that these PHEs result from photons emitted from a single location in LUX, the T-BA value of -0.3 indicates that the light source may reside right below the liquid surface or near the extraction grid. Alternatively, the photons may also come from fluorescence of the PTFE reflectors that surround the whole active xenon volume. PTFE fluorescence following VUV photon absorption has been reported [61], and may produce the observed T-BA value when appropriate weights are given to the fluorescence intensities from PTFE surfaces immersed in the liquid and in the gas.

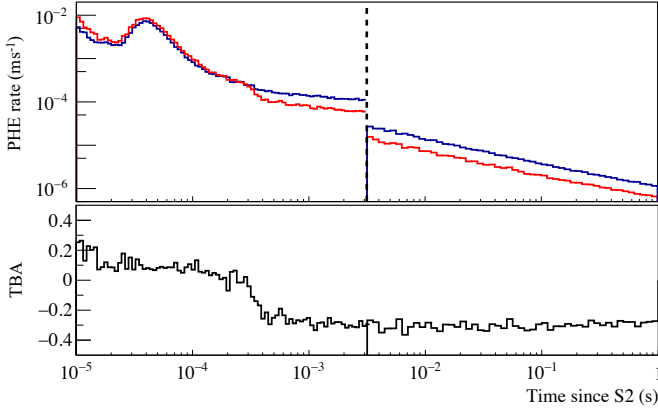


FIG. 11. **Top:** The PHE rate observed in the top (red) and bottom (blue) PMT array of LUX as a function of time since the preceding S2s. Due to the slower PHE rate decrease over time than that of SEs, larger contamination is expected from the photon tail of previous events, as indicated by the large discontinuity at 3 ms. **Bottom:** The top-bottom asymmetry (T-B-A) of the PHE pulses as a function of time since S2s. In LUX, S1 PMT signals have a T-B-A value of -0.3 (near liquid surface) to -0.8 (near cathode), and S2 has an average T-B-A value of 0.16 .

Contrary to the electron backgrounds, the PHE rate does not significantly depend on the impurity concentration in liquid xenon, or the position of the preceding interaction event (either X-Y or Z). The PHE rate also decreases more slowly with time than the SE rate. Therefore, we may rule out the possibility of these photons being emitted as a by-product of the electron emission process but, instead, they may be a triggering mechanism for electron emission through photoionization of negatively charged impurities. The different slopes of the rate decay for the PHEs and SEs might be explained as the depletion of relevant negative ion species over time. Due to the unknown photon wavelength and thus the uncertain PMT quantum efficiency at this wavelength, we cannot directly compare the electron-to-photon rate in this analysis to the photoionization yield by VUV xenon light discussed in Sec. IV.

VII. DISCUSSION

As noted from Sec. III to Sec. VI, the majority of background electrons observed in LUX demonstrate strong time, energy and position correlations with previous particle interactions in the detector. Therefore, they can be substantially suppressed through a veto cut after high energy events. Figure 12 (left) shows the residual electron event rate in ten days of LUX WIMP-search data using two veto algorithms: the first method (red histogram) uses a simple 50 ms veto cut after each identified interaction of 1 keV or above; the second (blue histogram) employs an aggressive veto cut of 50 ms–5 s, determined by the energy and depth of the event (considering the

power-law form in Figure 9). The live-time loss due to the veto cut is 13% for the first method and 90% for the second. In addition to the veto cut, we require no other S2 or SE pulses, or S1 pulses of greater than 3 PHE, in the same event window ($350 \mu\text{s}$) as the pulses of interest. Additional efficiency losses due to this cut are estimated to be less than 5%. The data selected have relatively high and stable liquid xenon purity ($900\text{--}950 \mu\text{s}$ electron lifetime), which, as discussed in Sec. VI, leads to less delayed electron emission.

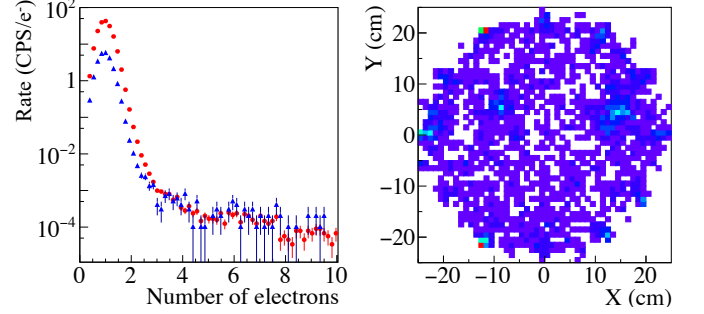


FIG. 12. **Left:** Residual electron event rate (livetime corrected) in 10 days of LUX dark matter search data with a conservative (red) and an aggressive veto cut (blue) after events of >1 keV (more explanations on the cut methods can be found in the text); intense periods of hot-spot electron emission (shown in the right figure) have been excluded; **Right:** The X-Y position distribution of residual electron pulses above 2.5 extracted electrons. The hot spots in the inner volume are attributed to grid electron emission.

As a result of their high rate, SEs dominate the electron spectra even after the veto cuts. With a 50 ms veto, the livetime-corrected rate of SEs is 26 CPS, and it decreases to 4 CPS with the aggressive veto cut in the second method. Because of the slow decay (Figure 9), the post-veto SE rate is expected to continue to decrease for longer veto windows if they can be afforded. Above the SE tail of $2.5 e^-$, the rate of electron events drops by a factor of $10^4\text{--}10^5$ and these values appear to be insensitive to changes of veto windows.

Figure 12 (right) shows the X-Y position distribution of multiple-electron (ME) pulses after the veto cuts. In contrast to the residual SEs that are approximately uniformly distributed in the X-Y space, MEs are observed to congregate at the edge and also some inner regions of the detector. A temporal study revealed that the majority of spatially congregated ME pulses in the inner volume emerged in bursts during short emission periods of 1–50 seconds. Similar transient electron emission from hot spots have also been reported in Ref. [42] and [24], and are attributed to grid emission. A total of three substantial rate spikes are observed in this 10-day data set, and a few additional ones with smaller amplitudes can be seen but these might also be explained as statistical fluctuations of the background rate. Given its frequent occurrence and varying amplitude, grid electron emission can be responsible for a significant fraction of the residual

electron events in LUX.

Although electron emission from metal surfaces is usually expected to produce SEs, electron multiplication can occur in high field regions [62] near physical or chemical defects, which explains the ME pulses in the intense grid emission periods. Such a multiplication effect was observed in LUX during a grid conditioning campaign that took place in 2014 between WS2013 and WS2014–16, when the high voltage on the LUX extraction grid was increased to past the onset of intense electron emission [42]. During normal LUX operations, the grid voltage was reduced to avoid spurious electron emission and high voltage instabilities. However, this observation of electron rate spikes from hot spots suggests that the grid emission pathology still plays a significant role in LUX, and possibly in other experiments that appear to maintain stable high voltage operations.

With an illustrative fiducial cut of $r < 12$ cm, the ME rate in Figure 12 (left) is reduced by another factor of 2 to 30–40 events/ton/day/e[−]. This rate is approximately 10 times higher than that reported by XENON1T at 4.5 extracted electrons [20], but we emphasize that this analysis, which focuses on the characterization of electron background in dual-phase xenon TPCs such as LUX, does not investigate all possible background rejection methods. For example, the shape of S2 pulses has been demonstrated to be a powerful tool in rejecting ME events from electrode grids [20, 63], so a dedicated ionization-only analysis with LUX data can lead to higher sensitivity to light dark matter interactions than that inferred from Figure 12 (left). In addition, a rigorous evaluation of all relevant efficiencies in this alternative LUX analysis is beyond the scope of this work.

This characterization of background electrons in LUX provides useful guidance for future experimental and analytical work that searches for low energy interactions in dual-phase xenon TPCs. For an experiment that focuses on the single- to few-electron region, it will be crucial to achieve an excellent liquid xenon purity to mitigate the long-lasting emission of impurity-captured electrons. This may be achieved by eliminating all high-outgassing materials from the active xenon volume or by isolating the clean xenon from critical detector components that may outgas significantly [64, 65]. It is worth noting that as the liquid xenon purity increases, delayed emission of trapped electrons under the liquid surface can occur at larger time delays from preceding energy depositions, and a veto method as discussed in this analysis may become inefficient. Instead, a high electron extraction efficiency close to 100% will be beneficial [14]. In addition, surface treatments for the electrode grids, such as passivation, will be necessary to reduce the emission of single- to multiple-electron pulses from grid surfaces under high electric fields [24]. For large detectors with a fine position resolution, spatial X-Y cuts after high energy events can be implemented to part of the detector in a veto analysis to avoid unnecessary loss of exposure, thanks to the strong position correlation between major back-

ground populations and preceding interactions.

VIII. CONCLUSION

We report a comprehensive description of all major electron background pathologies observed in the LUX dark matter detector, including both clustered electron emission and individual electron emission. The dominant electron background can be attributed to ionization phenomena resulting from previous energy depositions in the detector based on their position and energy correlations. By investigating the behavior of each electron background population under different experimental conditions, we propose that these electrons may be explained by the photoelectric effect of xenon scintillation and electroluminescence light, delayed emission of trapped electrons at the liquid surface, the excited emission of electrons captured by electronegative impurities, and cathodic electrode surface emission. Therefore, the background will be substantially reduced with a high electron extraction efficiency, a pure liquid xenon target, surface treatments of electrode grids, and a time veto after high energy deposits in the detector. Future dual-phase xenon TPC experiments that implement these experimental and analytical methods can be expected to achieve high sensitivities in searches of low-mass dark matter interactions.

ACKNOWLEDGMENTS

This work was partially supported by the U.S. Department of Energy (DOE) under Award No. DE-AC02-05CH11231, DE-AC05-06OR23100, DE-AC52-07NA27344, DE-FG01-91ER40618, DE-FG02-08ER41549, DE-FG02-11ER41738, DE-FG02-91ER40674, DE-FG02-91ER40688, DE-FG02-95ER40917, DE-NA0000979, DE-SC0006605, DE-SC0010010, DE-SC0015535, and DE-SC0019066; the U.S. National Science Foundation under Grants No. PHY-0750671, PHY-0801536, PHY-1003660, PHY-1004661, PHY-1102470, PHY-1312561, PHY-1347449, PHY-1505868, and PHY-1636738; the Research Corporation Grant No. RA0350; the Center for Ultra-low Background Experiments in the Dakotas (CUBED); and the South Dakota School of Mines and Technology (SDSMT).

Laboratório de Instrumentação e Física Experimental de Partículas (LIP)-Coimbra acknowledges funding from Fundação para a Ciência e a Tecnologia (FCT) through the Project-Grant PTDC/FIS-NUC/1525/2014. Imperial College and Brown University thank the UK Royal Society for travel funds under the International Exchange Scheme (IE120804). The UK groups acknowledge institutional support from Imperial College London, University College London and Edinburgh University, and from the Science & Technology Facilities

Council for PhD studentships R504737 (EL), M126369B (NM), P006795 (AN), T93036D (RT) and N50449X (UU). This work was partially enabled by the University College London (UCL) Cosmoparticle Initiative. The University of Edinburgh is a charitable body, registered in Scotland, with Registration No. SC005336.

This research was conducted using computational resources and services at the Center for Computation and Visualization, Brown University, and also the Yale Science Research Software Core.

We gratefully acknowledge the logistical and technical support and the access to laboratory infrastructure pro-

vided to us by SURF and its personnel at Lead, South Dakota. SURF was developed by the South Dakota Science and Technology Authority, with an important philanthropic donation from T. Denny Sanford. SURF is a federally sponsored research facility under Award Number DE-SC0020216.

J. Xu is partially supported by the U.S. DOE Office of Science, Office of High Energy Physics under Work Proposal Numbers SCW1676 and SCW1077 awarded to Lawrence Livermore National Laboratory (LLNL). LLNL is operated by Lawrence Livermore National Security, LLC, for the U.S. Department of Energy, National Nuclear Security Administration under Contract DE-AC52-07NA27344.

-
- [1] B. Edwards, H. M. Araújo, V. Chepel, D. Cline, T. Durkin, J. Gao, C. Ghag, E. V. Korolkova, V. N. Lebedenko, A. Lindote, et al., *Astroparticle Physics*, **30**, 54 (2008), ISSN 0927-6505.
 - [2] S. Sangiorgio, T. Joshi, A. Bernstein, J. Coleman, M. Foxe, C. Hagmann, I. Jovanovic, K. Kazkaz, K. Mavrokoridis, V. Mozin, et al., *Nuclear Instruments and Methods in Physics Research Section A: Accelerators, Spectrometers, Detectors and Associated Equipment*, **728**, 69 (2013), ISSN 0168-9002.
 - [3] J. Tiffenberg, M. Sofo-Haro, A. Drlica-Wagner, R. Essig, Y. Guardincerri, S. Holland, T. Volansky, and T.-T. Yu, *Phys. Rev. Lett.*, **119**, 131802 (2017).
 - [4] R. K. Romani, P. L. Brink, B. Cabrera, M. Cherry, T. Howarth, N. Kurinsky, R. A. Moffatt, R. Partridge, F. Ponce, M. Pyle, et al., *Applied Physics Letters*, **112**, 043501 (2018).
 - [5] E. Boulton, E. Bernard, N. Destefano, B. Edwards, M. Gai, S. Hertel, M. Horn, N. Larsen, B. Tennyson, C. Wahl, et al., *Journal of Instrumentation*, **12**, P08004 (2017).
 - [6] D. S. Akerib, S. Alsum, H. M. Araújo, X. Bai, A. J. Bailey, J. Balajthy, P. Beltrame, E. P. Bernard, A. Bernstein, T. P. Biesiadzinski, et al., *Phys. Rev. D*, **96**, 112011 (2017).
 - [7] B. G. Lenardo, J. Xu, S. Pereverzev, O. A. Akindele, D. Naim, J. Kingston, A. Bernstein, K. Kazkaz, M. Tripathi, C. Awe, et al., *Phys. Rev. Lett.*, **123**, 231106 (2019).
 - [8] C. Monteiro, L. Fernandes, J. Lopes, L. Coelho, J. Veloso, J. dos Santos, K. Giboni, and E. Aprile, *Journal of Instrumentation*, **2**, P05001 (2007).
 - [9] E. Santos, B. Edwards, V. Chepel, H. M. Araújo, D. Y. Akimov, E. J. Barnes, V. A. Belov, A. A. Burenkov, A. Currie, L. DeViveiros, et al. (ZEPLIN-III Collaboration), *Journal of High Energy Physics*, **2011**, 115 (2011), ISSN 1029-8479.
 - [10] J. Angle, E. Aprile, F. Arneodo, L. Baudis, A. Bernstein, A. I. Bolozdynya, L. C. C. Coelho, C. E. Dahl, L. DeViveiros, A. D. Ferella, et al. (XENON10 Collaboration), *Phys. Rev. Lett.*, **107**, 051301 (2011).
 - [11] E. Aprile, M. Alfonsi, K. Arisaka, F. Arneodo, C. Balan, L. Baudis, B. Bauermeister, A. Behrens, P. Beltrame, K. Bokeloh, et al., *Journal of Physics G: Nuclear and Particle Physics*, **41**, 035201 (2014).
 - [12] D. S. Akerib, S. Alsum, H. M. Araújo, X. Bai, A. J. Bailey, J. Balajthy, P. Beltrame, E. P. Bernard, A. Bernstein, T. P. Biesiadzinski, et al. (LUX Collaboration), *Phys. Rev. D*, **97**, 102008 (2018).
 - [13] B. Edwards, E. Bernard, E. Boulton, N. Destefano, M. Gai, M. Horn, N. Larsen, B. Tennyson, L. Tvrznikova, C. Wahl, et al., *Journal of Instrumentation*, **13**, P01005 (2018).
 - [14] J. Xu, S. Pereverzev, B. Lenardo, J. Kingston, D. Naim, A. Bernstein, K. Kazkaz, and M. Tripathi, *Phys. Rev. D*, **99**, 103024 (2019).
 - [15] R. Essig, A. Manalaysay, J. Mardon, P. Sorensen, and T. Volansky, *Phys. Rev. Lett.*, **109**, 021301 (2012).
 - [16] R. Essig, T. Volansky, and T.-T. Yu, *Phys. Rev. D*, **96**, 043017 (2017).
 - [17] Peter Sorensen, [arXiv:1702.04805](https://arxiv.org/abs/1702.04805) (2017).
 - [18] P. Sorensen and K. Kamdin, *Journal of Instrumentation*, **13**, P02032 (2018).
 - [19] D. S. Akerib, S. Alsum, H. M. Araújo, X. Bai, A. J. Bailey, J. Balajthy, P. Beltrame, E. P. Bernard, A. Bernstein, T. P. Biesiadzinski, et al. (LUX Collaboration), *Phys. Rev. D*, **95**, 012008 (2017).
 - [20] E. Aprile, J. Aalbers, F. Agostini, M. Alfonsi, L. Althueser, F. D. Amaro, V. C. Antochi, E. Angelino, F. Arneodo, D. Barge, et al. (XENON Collaboration), *Phys. Rev. Lett.*, **123**, 251801 (2019).
 - [21] D. S. Akerib, S. Alsum, H. M. Araújo, X. Bai, J. Balajthy, A. Baxter, P. Beltrame, E. P. Bernard, A. Bernstein, T. P. Biesiadzinski, et al. (LUX Collaboration), *Phys. Rev. D*, **101**, 042001 (2020).
 - [22] B. Edwards, Ph.D. thesis, Imperial College London (2009), URL <https://spiral.imperial.ac.uk/8443/handle/10044/1/5540>.
 - [23] J. J. Chapman, Ph.D. thesis, Brown U. (2014), URL <https://doi.org/10.7301/Z0BV7DZZ>.
 - [24] A. Tomás, H. M. Araújo, A. J. Bailey, A. Bayer, E. Chen, B. López-Paredes, and T. J. Sumner, *Astroparticle Physics*, **103**, 49 (2018), ISSN 0927-6505.
 - [25] D. Akimov, V. Belov, A. Bolozdynya, Y. Efremenko, A. Etenko, A. Galavanov, D. Gouss, Y. Gusakov, D. Kdib, A. Khromov, et al., [arXiv:1910.06190](https://arxiv.org/abs/1910.06190) (2019).
 - [26] D. Akerib, X. Bai, S. Bedikian, E. Bernard, A. Bernstein, A. Bolozdynya, A. Bradley, D. Byram, S. Cahn,

- C. Camp, et al., *Nuclear Instruments and Methods in Physics Research Section A: Accelerators, Spectrometers, Detectors and Associated Equipment*, **704**, 111 (2013), ISSN 0168-9002.
- [27] D. S. Akerib, H. M. Araújo, X. Bai, A. J. Bailey, J. Balajthy, S. Bedikian, E. Bernard, A. Bernstein, A. Bolozdynya, A. Bradley, et al. (The LUX Collaboration), *Phys. Rev. Lett.*, **112**, 091303 (2014).
- [28] D. S. Akerib, H. M. Araújo, X. Bai, A. J. Bailey, J. Balajthy, P. Beltrame, E. P. Bernard, A. Bernstein, T. P. Biesiadzinski, E. M. Boulton, et al. (LUX Collaboration), *Phys. Rev. Lett.*, **116**, 161301 (2016).
- [29] D. S. Akerib, S. Alsum, H. M. Araújo, X. Bai, A. J. Bailey, J. Balajthy, P. Beltrame, E. P. Bernard, A. Bernstein, T. P. Biesiadzinski, et al. (LUX Collaboration), *Phys. Rev. Lett.*, **118**, 021303 (2017).
- [30] D. S. Akerib, H. M. Araújo, X. Bai, A. J. Bailey, J. Balajthy, P. Beltrame, E. P. Bernard, A. Bernstein, T. P. Biesiadzinski, E. M. Boulton, et al. (LUX Collaboration), *Phys. Rev. D*, **93**, 072009 (2016).
- [31] D. S. Akerib, S. Alsum, H. M. Arajo, X. Bai, A. J. Bailey, J. Balajthy, P. Beltrame, E. P. Bernard, A. Bernstein, T. P. Biesiadzinski, et al. (LUX Collaboration), *arXiv:1608.05381* (2016).
- [32] D. S. Akerib, S. Alsum, H. M. Araújo, X. Bai, A. J. Bailey, J. Balajthy, P. Beltrame, E. P. Bernard, A. Bernstein, T. P. Biesiadzinski, et al. (LUX Collaboration), *Phys. Rev. D*, **96**, 112009 (2017).
- [33] D. S. Akerib, S. Alsum, H. M. Araújo, X. Bai, A. J. Bailey, J. Balajthy, P. Beltrame, E. P. Bernard, A. Bernstein, T. P. Biesiadzinski, et al., *Journal of Instrumentation*, **13**, P02001 (2018).
- [34] D. Akerib, X. Bai, S. Bedikian, E. Bernard, A. Bernstein, A. Bradley, S. Cahn, M. Carmona-Benitez, D. Carr, J. Chapman, et al., *Nuclear Instruments and Methods in Physics Research Section A: Accelerators, Spectrometers, Detectors and Associated Equipment*, **668**, 1 (2012), ISSN 0168-9002.
- [35] D. S. Akerib, S. Alsum, H. M. Araújo, X. Bai, A. J. Bailey, J. Balajthy, P. Beltrame, E. P. Bernard, A. Bernstein, T. P. Biesiadzinski, et al., *Journal of Instrumentation*, **12**, P11022 (2017).
- [36] E. Gushchin, A. Kruglov, V. Litskevich, A. Lebedev, I. M. Obodovskii, and S. Somov, *Journal of Experimental and Theoretical Physics*, **49**, 856 (1979).
- [37] R. Reininger, U. Asaf, and I. Steinberger, *Chemical Physics Letters*, **90**, 287 (1982), ISSN 0009-2614.
- [38] A. Bolozdynya, V. Egorov, B. Rodionov, and V. Miroshnichenko, *IEEE Transactions on Nuclear Science*, **42**, 565 (1995), ISSN 0018-9499.
- [39] L. W. Bruch, R. D. Diehl, and J. A. Venable, *Rev. Mod. Phys.*, **79**, 1381 (2007).
- [40] R. C. Monreal, *Progress in Surface Science*, **89**, 80 (2014), ISSN 0079-6816.
- [41] D. Huang, Ph.D. thesis, Brown U. (2019).
- [42] A. Bailey, Ph.D. thesis, Imperial College London (2016), URL <https://spiral.imperial.ac.uk/handle/10044/1/41878>.
- [43] B. Rebel, C. Hall, E. Bernard, C. H. Faham, T. M. Ito, B. Lundberg, M. Messina, F. Monrabal, S. P. Pereverzev, F. Resnati, et al., *Journal of Instrumentation*, **9**, T08004 (2014).
- [44] C. Faham, V. Gehman, A. Currie, A. Dobi, P. Sorensen, and R. Gaitskell, *Journal of Instrumentation*, **10**, P09010 (2015).
- [45] D. Akerib, X. Bai, S. Bedikian, E. Bernard, A. Bernstein, A. Bradley, S. Cahn, M. Carmona-Benitez, D. Carr, J. Chapman, et al., *Nuclear Instruments and Methods in Physics Research Section A: Accelerators, Spectrometers, Detectors and Associated Equipment*, **675**, 63 (2012), ISSN 0168-9002.
- [46] S. Agostinelli, J. Allison, K. Amako, J. Apostolakis, H. M. Araújo, P. Arce, M. Asai, D. Axen, S. Banerjee, G. Barrand, et al., *Nuclear Instruments and Methods in Physics Research Section A: Accelerators, Spectrometers, Detectors and Associated Equipment*, **506**, 250 (2003), ISSN 0168-9002.
- [47] COMSOL, Inc., *Comsol multiphysics* (2020), URL <https://www.comsol.com/comsol-multiphysics>.
- [48] B. Feuerbacher and B. Fitton, *Journal of Applied Physics*, **43**, 1563 (1971).
- [49] W. Tauchert and W. F. Schmidt, *Zeitschrift für Naturforschung*, **30**, 1085 (1975).
- [50] D. H. Dowell and J. F. Schmerge, *Phys. Rev. ST Accel. Beams*, **12**, 074201 (2009).
- [51] L. Malter, *Phys. Rev.*, **50**, 48 (1936).
- [52] K. Fujii, Y. Endo, Y. Torigoe, S. Nakamura, T. Haruyama, K. Kasami, S. Mihara, K. Saito, S. Sasaki, and H. Tawara, *Nuclear Instruments and Methods in Physics Research Section A: Accelerators, Spectrometers, Detectors and Associated Equipment*, **795**, 293 (2015), ISSN 0168-9002.
- [53] T. Takahashi, S. Himi, M. Suzuki, J. zhi Ruan(Gen), and S. Kubota, *Nuclear Instruments and Methods in Physics Research*, **205**, 591 (1983), ISSN 0167-5087.
- [54] O. Hilt, W. Schmidt, and A. Khrapak, *IEEE Transactions on Dielectrics and Electrical Insulation*, **1**, 648 (1994), ISSN 1558-4135.
- [55] D. Malling, Ph.D. thesis, Brown University (2014), URL <https://doi.org/10.7301/Z0057D9F>.
- [56] L. W. Goetzke, E. Aprile, M. Anthony, G. Plante, and M. Weber, *Phys. Rev. D*, **96**, 103007 (2017).
- [57] P. F. Sorensen, Ph.D. thesis, Brown U. (2008), URL http://pa.brown.edu/resources_files/theses/2008_Sorensen_Thesis.pdf.
- [58] P. Neves, C. Conde, and L. Távora, *Nuclear Instruments and Methods in Physics Research Section A: Accelerators, Spectrometers, Detectors and Associated Equipment*, **580**, 66 (2007), ISSN 0168-9002, proceedings of the 10 th International Symposium on Radiation Physics.
- [59] G. Bakale, U. Sowada, and W. F. Schmidt, *The Journal of Physical Chemistry*, **80**, 2556 (1976).
- [60] B. L. Smith, P. R. Gardner, and E. H. C. Parker, *Journal of Chemical Physics*, **47**, 1148 (1967).
- [61] P.-S. Shaw, Z. Li, U. Arp, and K. R. Lykke, *Appl. Opt.*, **46**, 5119 (2007).
- [62] G. Alkhazov, *Nuclear Instruments and Methods*, **89**, 155 (1970), ISSN 0029-554X.
- [63] P. Sorensen, *Nuclear Instruments and Methods in Physics Research Section A: Accelerators, Spectrometers, Detectors and Associated Equipment*, **635**, 41 (2011), ISSN 0168-9002.
- [64] K. Sato, M. Yamashita, K. Ichimura, Y. Itow, S. Kazama, S. Moriyama, K. Ozaki, T. Suzuki, and R. Yamazaki, *arXiv:1910.13831* (2019).
- [65] A. Bernstein, M. Clark, R. Essig, M. Fernandez-Serra, A. Kopec, R. Lang, J. Long, K. Ni, S. Pereverzev, J. Qi, et al., *arXiv:2001.09311* (2020).